IEEE Access
Multidisciplinary | Rapid Review | Open Access Journal

Received January 18, 2021, accepted January 28, 2021, date of publication February 10, 2021, date of current version February 22, 2021.

Digital Object Identifier 10.1109/ACCESS.2021.3058593

Stainless-Core Submersible Permanent Magnet Synchronous Machine

ALVARO E. HOFFER[1,2], (Student Member, IEEE), ILYA PETROV[1], JUHA J. PYRHÖNEN[1], (Senior Member, IEEE), AND JUAN A. TAPIA[2], (Senior Member, IEEE)

[1]Department of Electrical Engineering, LUT University, 53851 Lappeenranta, Finland
[2]Department of Electrical Engineering, University of Concepción, Concepción 4070386, Chile

Corresponding author: Alvaro E. Hoffer (alvaro.hoffer.garces@lut.fi)

This work was supported in part by the LUT University, Finland, and in part by the Agencia Nacional de Investigación y Desarrollo (ANID), Chile, through the Project FONDECYT Regular under Grant 1201667.

ABSTRACT A fully submersible permanent magnet synchronous machine (PMSM) is introduced in this paper. Underwater operation requires that the machine parts have to be resistant to corrosion, and the electrically conducting parts need to be properly insulated from water. The machine under study consists of a rotor-surface permanent magnet rotor, protected by a glass-fiber-reinforced plastic (GFRP) cover, and a fully stainless stator. The novelty of the machine is found in the design and special materials used in the manufacture. The stator core is made of ferritic stainless steel laminations, and the selected winding material is polyvinyl chloride (PVC) insulated copper wire. An extra low-speed, stainless-core submersible PMSM was constructed and tested. To simplify the machine construction, a tooth-coil single-layer winding was adopted. An asymmetric stator design was selected to enhance the machine performance. The performance of the 1.7 kW, 80 r/min machine was analyzed by finite element analysis (FEA) and validated by experimental tests, where despite a very low rotational speed, 74% efficiency was reached at the target load point. The PMSM was found to be fully functional for the application.

INDEX TERMS Asymmetrical stator, canned machine, finite element analysis, hysteresis torque, permanent magnets, permanent magnet machines, submersible machine, tooth-coil winding.

I. INTRODUCTION

Through this article, a stainless-core submersible permanent magnet synchronous machine (PMSM) as an alternative to a conventional submersible machine is discussed. The electromagnetic performance of submersible machines [1]–[3] has been a topic of numerous studies. In [1], a 12-slot 10-pole canned rotor surface magnet PMSM was studied. The motor structure has a metallic rotor can around the rotor permanent magnets (PMs) and a metallic stator can fixed to the inner side of the stator core. The cans are made of a Hastelloy C material, which is characterized as nonmagnetic and has a relatively high electrical resistivity. The fluid pumped into the machine can flow into the air gap between the rotor cans. The inevitable eddy currents induced in the cans increase the machine losses and reduce the air gap flux density. However, the higher order harmonics of the air gap flux density are also suppressed by the can eddy currents, which leads to a reduction in the permanent magnet losses. In [2], a flooded permanent magnet generator was investigated. The machine structure topology is the same as in the PMSM described in [1]. In this research, it was stated that the electrically conductive materials of the cans exhibit unavoidable eddy current losses, which leads to an increase in the temperature of the PM and the stator slots. However, when using nonconductive materials (e.g., fiberglass), the inside temperature of the PMs and the stator slots was lower than in the case with metallic cans (e.g., Stainless steel 304L, Inconel Alloy 718, or Titanium SP 700). In [3], a 15-slot 10-pole ferrite magnet spoke-type submersible brushless DC motor was introduced. The motor is characterized by a small diameter, a large axial length, and a low cost. Contrary to the above-mentioned motors, the brushless DC motor is insulated from water using an austenitic stainless steel frame and flanges, which

The associate editor coordinating the review of this manuscript and approving it for publication was Zhuang Xu.

means that water cannot penetrate into the air gap at all.

Using protective elements to enclose the active part of the machine from direct contact with water can be considered a common approach in submersible machines. However, these protection elements are susceptible to failure over time as a result of corrosion, leading to the reduced lifetime of the machine. On the other hand, there are soft magnetic materials, such as ferritic stainless steels, that are corrosion resistant and have acceptable magnetic properties [4]. Hence, these materials can, at least in some cases, be used as an alternative in the design of electrical machines, and they make it possible to completely avoid the use of protective covers and a casing seal.

In this work, a stainless-core submersible PMSM with rotor-surface magnets is proposed. The construction is preferred because of its favorable performance characteristics in low-speed high-torque applications. The stator core is made of ferritic stainless steel sheets. The use of this steel type is normally limited to certain applications, such as the automotive sector and industrial equipment. However, the use of such this material is not common in electrical machines, especially in the manufacture of the magnetic core. Therefore, this study could be an important step toward the investigation of the use of a stainless-steel core in submersible permanent magnet machines.

To avoid early interruptions caused by a winding contact with water, extra protection for the winding is required [5]. The selected winding material is polyvinyl chloride (PVC) insulated copper wire. The rotor materials (PMs and rotor core) are not resistant to corrosion. Therefore, a glass-fiber-reinforced plastic (GFRP) cover is mounted on the PMs facing the air gap, and all the empty space below the rotor cover (e.g., gaps between the magnets or some air voids) is filled with water-proof epoxy resin. The rotor cover material is required in order to avoid additional losses in contrast to metallic covers [1], [2]. The rotor ends and the shaft are made of austenitic stainless steel.

The use of a completely encapsulated traditional stator was avoided because of the complex structure and poor heat transfer properties of the stator. The stator has more active elements, and it is surrounded by water from the outer and inner surfaces. Instead, the rotor is a relatively simple component and surrounded by water only from the outer surface, which makes it easier to use a cover (with filled resin all over the rotor body) to protect it. Furthermore, if the rotor cover fails, the machine performance will not be affected immediately if coated magnets are used. In contrast, if water penetrates the stator, it will soon lead to a winding earth failure because of the thin layer of wire insulation. Therefore, this makes encapsulation of the stator much more challenging and less reliable.

The fractional-slot concentrated nonoverlapping winding, also known as the tooth-coil winding (TCW) is the winding type that has gained in interest among researchers and is frequently used in PMSMs [6]–[10]. The interest in this winding type is explained by its inherent advantages, such as a short end-winding length, easiness and low cost of manufacture, and good fault tolerance [11], [12]. Moreover, asymmetric stator configuration features can be exploited by adopting a TCW configuration to improve the machine performance [13]–[15]. Despite its advantages, the TCW also exhibits a large harmonic spectrum of the current linkage waveform, which has a negative impact on the machine in the form of high rotor losses. Nevertheless, there are methods to mitigate this effect, e.g., choosing rotor materials with a high electrical resistivity.

The main contribution of the paper is to analyze and verify the behavior of a submersible motor. The winding type selected in this application is the TCW because of its considerable advantages, especially in manufacture. The machine design process is based on qualitative observations and the algorithm proposed in [16]. An optimization process is carried out where the stator tooth inner width that carries a coil is adjusted while maintaining the stator slot width.

As a continuation of the preliminary work presented in [17], this paper develops a more comprehensive design approach and a different application scenario (motor mode). Even though the design process is straightforward, this paper provides valuable information, e.g., on the performance of a machine manufactured from nontraditional materials along with the use of a nonsymmetrical stator structure.

The paper is organized as follows. In Section II, the design of the PMSM is described. This section addresses the choice of the number of slots and poles, material selection, design guidelines, and asymmetric stator features. In Section III, a numerical evaluation of the machine is carried out. A performance comparison is made with a canned stator machine with similar dimensions but using traditional electrical steel to demonstrate the advantages and disadvantages of the proposed machine. The machine is constructed according to the requirements imposed by the application, which are explained later in the paper. Section IV provides some details of the machine manufacture and measurement of certain machine characteristics to validate the functionality of the machine when submerged in a water tank. Finally, Section V concludes the results.

II. DESIGN OF THE STAINLESS STEEL CORE SUBMERSIBLE PMSM

The application comprises an axial-flow impeller coupled directly to a PMSM as presented in Fig. 1. These elements constitute a pump system, which is operated submerged in lake water in a vertical arrangement. The motor itself is implemented as a fully open construction allowing lake water to penetrate its water-lubricated bearings and the air gap, and thereby provide efficient cooling. No vulnerable shaft seals are needed. The function of the pump is to deliver oxygen-rich surface water to the lake bottom to mitigate eutrophication problems in the lake. More detailed description of the pumping system is not relevant to the design aspects of the PMSM, and it is thus beyond the scope of this paper.

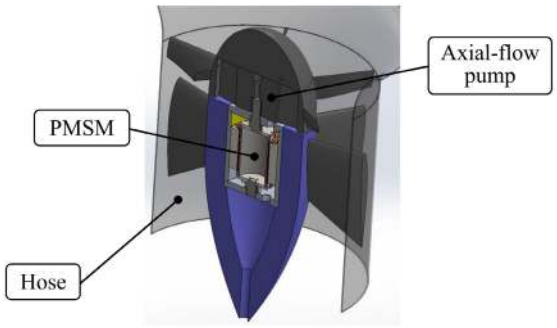

FIGURE 1. Cross-sectional view of the axial-flow pump impeller with the integrated PMSM.

TABLE 1. Machine specifications.

Parameter	Value
Rated torque T_N (Nm)	202
Maximum torque T_N (Nm)	283
Rated power P_N (W)	1700
Rated mechanical speed n_N (rpm)	80
Rated stator frequency f_{sN} (Hz)	13⅓

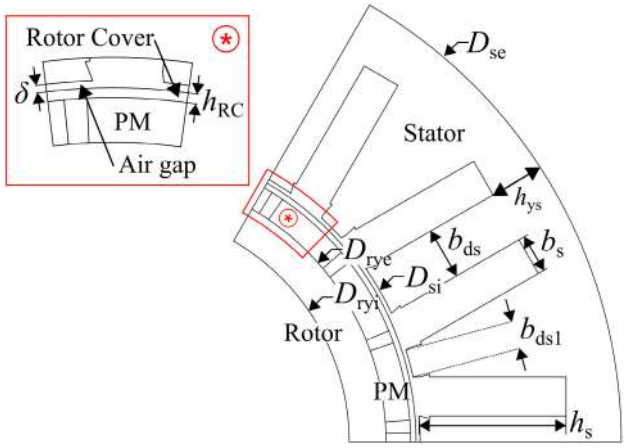

FIGURE 2. Cross-sectional view of the submersible core PMSM.

The machine is a radial-flux-inner-rotor PMSM. The rotor surface magnet configuration is preferred for its simplicity and more accessible construction when a simple solid rotor core is applied [18]. The stator external diameter D_{se} and the stator stack length l of the machine are set to 369.9 mm and 300 mm, respectively, according to the application requirements. The target specifications of the machine are given in Table 1. A cross-sectional view of the PMSM is illustrated in Fig. 2.

A. SELECTION OF THE NUMBER OF POLES AND SLOTS

As mentioned in the Section I, a single-layer TCW is adopted to simplify the manufacture and enhance the machine reliability as every coil remains separated from other coils. However, for a three-phase winding, the number of combinations of the number of slots Q_s and poles $2p$ is limited because of the number of slots per pole and phase in tooth-coil machines is $q \leq 0.5$. There are several quality indices to predict the performance of the machine according to the selected slot–pole combination, such as the fundamental winding pitch factor k_{pp}, the air gap harmonic leakage factor σ_δ, and the mutual coupling factor m_c [7], [9], [19]. To avoid unbalanced magnetic pull, it should be ensured that the greatest common divisor GCD(Q_s, $2p$) has a high and even value. To reduce the cogging torque, the least common multiple LCM(Q_s, $2p$) should have a high value [9]. The choice of the winding configuration should be based mainly on the number of poles, the air gap leakage factor, and the mutual inductance coefficient [7].

TCW technology offers several advantages over other winding configurations. It, however, exhibits a high content of spatial harmonics in the current linkage waveform, which has a significant influence on the rotor losses [20]. The content of spatial harmonics depends on q, where a certain trade-off between the losses generated in the rotor and extra losses in the stator winding can be observed.

The stator slot opening is selected to achieve a simple and safe assembly of the prefabricated coils. However, the open slot effect reduces the amplitude of the air gap flux density fundamental [21]. Therefore, it is necessary to choose a slot–pole combination with a high pitch factor without neglecting the other indices. A method to compensate for the penalties of the slot opening is to use asymmetric stator features. This may increase the pitch factor required to maximize the flux linkage and torque [13]. The single-layer winding is, in particular, applicable with an asymmetric stator structure [14]. The procedure for the stator asymmetry is explained in more detail later in this section.

Table 2 provides a comparison of feasible slot–pole combinations based on previous considerations. Note that when multiple poles are used, it is possible to reduce the eddy current rotor losses compared with a lower number of poles; therefore, a higher pole number is chosen [22]. From the thermal point of view, a machine with a large number of narrow slots is preferred to improve the heat transfer [8]. As shown in Table 2, the best combination is found at 24 slots and 20 poles because of its high pitch factor, no magnetic coupling between the phases, and moderate air gap harmonic flux leakage. As the selected winding configuration does not guarantee the lowest rotor losses, it is necessary to choose rotor materials with a high electrical resistivity if the operating frequency is high.

B. MATERIALS SELECTION

Because of the submersible operation, the materials must be waterproof, or if not, they should be protected from direct contact with water, e.g., by a water protective cover. For the rotor yoke, constructional steel S355 was selected, as it exhibits acceptable magnetic and mechanical properties [23]. Naturally, it would be preferable to employ a laminated rotor core to limit the eddy current losses induced by the current linkage harmonics when a TCW is used, but because of the low operating frequency of $13^1/_3$ Hz and the relatively low

TABLE 2. Possible single-layer TCW slot–pole combinations.

Parameter	$Q_s/2p$			
	18/16	24/16	18/20	**24/20**
q	0.375	0.5	0.3	**0.4**
f_s[1]	10⅓	10⅓	13⅓	**13⅓**
k_{pp}[2]	0.9452	0.8660	0.9452	**0.9659**
σ_δ	1.20	0.46	0.46	**0.96**
m_c	-0.039	-0.5	-0.039	**0**
LCM(Q_s, $2p$)	144	48	180	**120**
GCD(Q_s, $2p$)	2	8	2	**4**

[1]Fundamental stator frequency (Hz).
[2]Fundamental winding pitch factor.

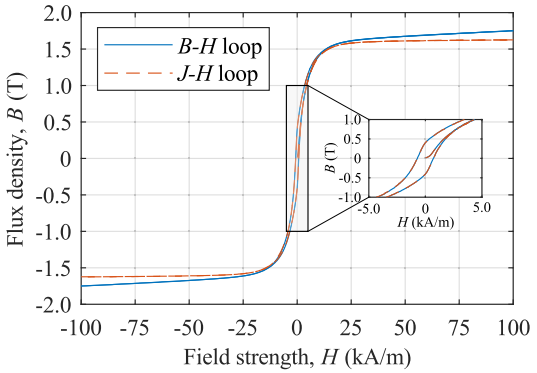

FIGURE 3. Magnetization curves of 430SS.

frequency caused by the slot opening permeance variations at the rated speed (which eliminates the risk of high rotor losses), a simple rotor core made of constructional steel tube is advisable, as it significantly simplifies the rotor manufacture.

In a rotor-surface-magnet PMSM with fixed rotor core dimensions, the air gap diameter D_s depends on the PM height h_{PM} [24]. Therefore, to limit the size of the machine and enhance the magnetic flux, the magnet material must have a high remanent flux density. For the present case, N45SH Neodymium Magnet was selected. N45SH has a remanent flux density of $B_r = 1.35$ T at an operating temperature of 20 °C. Moreover, it has a high coercive force to avoid a risk of irreversible demagnetization in a fault condition even if the temperature of the magnets exceeds 100 °C [25].

The rotor yoke and the PM material are not resistant to direct continuous contact with water, and therefore, a cover installed between the PMs and the water-filled gap is required. The material selected to cover the magnets is GFRP, which is nonmagnetic, fully resistant to corrosion, and has an ultralow electrical conductivity.

The stator core was made of 430 stainless steel grade (430SS) which is a ferritic stainless steel that has excellent intergranular corrosion resistance, acceptable magnetic and good mechanical properties, and a good market availability [4]. The magnetic properties of 430SS were measured with a hysteresigraph following the procedure shown in [26]. The magnetization curves of 430SS are shown in Fig. 3.

TABLE 3. Manufacturer data of the stator core materials.

Parameter	430SS	M400-50A
Flux density at 20 kA/m field strength (T)	1.58	2.00
Coercivity H_c (A/m)	708	50
Electrical resistivity σ ($\mu\Omega$m)	60	42
Lamination thickness d (mm)	1.0	0.5
Density ρ (kg/m^3)	7750	7700

For the winding material, low-cost PVC-insulated wires with solid conductors were selected, because they provide high-quality insulation and are entirely water-resistant.

To present the advantages and disadvantages of the proposed machine, a performance comparison with a canned stator machine was conducted. The canned stator machine has a cover structure similar to the rotor of the proposed machine, avoiding a direct contact of the active electromagnetic components with water, while the stator core is made of electrical steel M400-50A. The machine exhibits excellent magnetic and electrical characteristics, and it is also widely used in the manufacture of electrical machines. However, it is not resistant to corrosion, which explains the cover installation between the air gap region and the stator core. The cover material is the same as the rotor cover, GFRP.

The manufacturer data of 430SS and M400-50A are given in Table 3. The parameters of the electric steel M400-50A are known [27]; however, the magnetic parameters of the ferritic stainless steel are not provided by the manufacturer, and therefore, they are reported based on the magnetization measurements carried out in the present study.

C. DESIGN GUIDELINES

As it was mentioned at the beginning of this section, the main boundary conditions are the stator outer diameter D_{se} and the axial length l. The rotor yoke inner diameter D_{ryi} is fixed to 170 mm because of the size of the steel tube available. The electromagnetic design guidelines are as follows:

1) The rotor yoke height h_{yr} is designed to avoid saturation in the yoke.
2) The PM material is used efficiently because of its high cost. Therefore, the PM height h_{PM} is adjusted to maximize the no-load air gap flux density before the magnet BH load point gets too close to its remanence. The PM width w_{PM} is a result of the pole pitch width and some reasonable gap distance between the magnets to minimize the leakage between them.
3) The rotor cover thickness h_{RC} is chosen to be 2.0 mm to achieve the required mechanical stiffness and provide adequate protection for the magnetic parts [2], [28].
4) The physical air gap length δ_{phys} is chosen to be 1.5 mm, resulting in a magnetic air gap of $\delta = 3.5$ mm. The relatively large air gap length is preferred for easier and safer assembly if the rotor cover has not perfect shape. Further, it helps in achieving good heat transfer between the stator core and the water flowing in the air gap, and in reducing the harmonic content in the

TABLE 4. Machine parameters.

Parameter	Value
Number of turns per phase N_{ph}	232
Copper space factor k_{Cu}	0.27
Resistance factor k_R @ f_{sN}	~1.0
Stator outer diameter D_{se} (mm)	369.9
Stator inner diameter D_{si} (mm)	222.1
Rotor yoke outer diameter D_{rye} (mm)	197.1
Rotor yoke inner diameter D_{ryi} (mm)	170.0
Stator slot width b_s (mm)	14.25
Stator slot height h_s (mm)	54
Stator stack length l (mm)	300.0
PM width w_{PM} (mm)	27.4
PM height h_{PM} (mm)	9

air gap flux density produced by the armature reaction. Further, it should be noted that the cogging torque (peak-to-peak value) can be reduced with a long air gap.

5) The stator slot dimensions are selected together with the stator tooth inner width b_{ds} to avoid any high flux density in the slot. When using open slots, the slotting effect has a significant impact on the performance of the machine [21]. Therefore, the stator slot width b_s is chosen to be as narrow as possible to fit the preformed coils.
6) The stator yoke depth h_{ys} is selected so that the flux density within the stator yoke does not reach saturation, and an appropriate mechanical rigidity and efficient use of material are achieved.
7) The machine is designed to operate in the maximum torque per ampere (MTPA) region.

The machine main parameters (see Table 4) are obtained by using the design guidelines given above and the algorithm presented in [16]. The finite element analysis (FEA) model of the machine under study was implemented as a transient magnetic simulation in Flux by Altair. The machine was simulated in the 2D and skew simulation environments.

D. ASYMMETRIC STATOR FEATURES

Asymmetric features can be exploited by adopting the TCW configuration to enhance the machine performance. The aim of using unequal teeth widths is to increase the flux linkage. The procedure involves increasing every second stator tooth width and, to the same extent, reducing the adjacent stator tooth width, as shown in Fig. 4. The advantages of this asymmetry are given below.

One of the most critical parameters of a PMSM is the induced no-load voltage, also known as back-EMF. As reported in various studies [6], [8], [14], [29], it has a direct effect on machine performance. The RMS back-EMF can be expressed in simple terms as

$$E_{ph} = \frac{1}{\sqrt{2}} k_w \omega N_{ph} \Phi, \tag{1}$$

where ω is the electrical angular frequency, N_{ph} is the number of turns in series per phase, and Φ is the magnetic flux. The coil pitch W (see Fig. 4) depends on the distance between

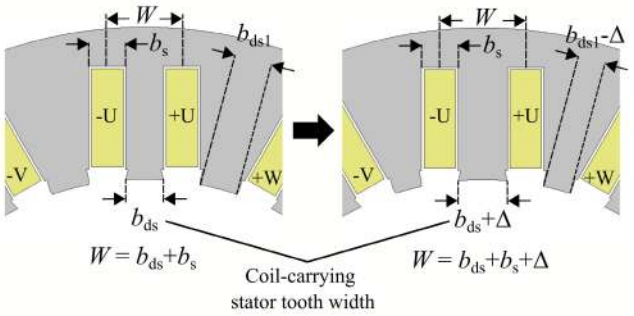

FIGURE 4. Adjustment procedure of the stator tooth inner width b_{ds}. The stator slot width b_s is kept constant.

the tooth that carries the coil b_{ds} and the slot width b_s. Therefore, increasing the coil-carrying stator tooth width makes it possible to increase the pitch factor k_p, and thereby, the winding factor k_w. From the electromagnetic point of view, it is possible to achieve a reduction in the RMS stator supply current I_s to reach the same electromagnetic torque by using asymmetry, because the torque is proportional to the product $E_{ph}I_s$. Moreover, it can lead to significant winding material savings, especially when the machine is large.

The use of stator asymmetry has a significant impact on the torque response of the machine. Fig. 5 shows the cogging torque as a function of rotor position at different tooth widths and its spectra. The cogging torque variation (peak-to-peak value) as a function of the stator tooth inner width b_{ds} is shown in Fig. 6. It can be seen that the variation of the stator tooth inner width b_{ds} affects the cogging torque. As Fig. 5(b) shows, the 6th-order cogging torque harmonic is the strongest harmonic component because of the asymmetric stator structure. To eliminate this particular harmonic (6th-order), the continuous skew angle to be applied is provided by

$$\theta_{skew} = \frac{2\pi}{\mathrm{LCM}\left(\frac{Q_s}{2}, 2p\right)}. \tag{2}$$

The factor $1/2$ that multiplies the number of slots Q_s in (2) is due to the different stator core geometry compared with the original symmetrical stator core shape. It is worth remembering that if the air gap length is reduced, the fundamental cogging torque harmonic $(Q_s, 2p)$ could occur (12th-order harmonic). Therefore, the use of stator asymmetries may not be suitable for thin air gaps and open slots. Finally, to eliminate the 6th-order harmonic along with the potential torque ripple harmonic, a two-step rotor skewing $(n_{step} = 2)$ with a shift of three mechanical degrees $(\theta_{skew}/n_{step} = 6/2 = 3$ degrees$)$ between the magnet layers was adopted.

III. NUMERICAL ANALYSIS

In this section, first, the procedure for calculating the machine losses is outlined. Then, the performance of the submersible core machine is verified and analyzed with the design guidelines, and the selection of materials is presented. Finally,

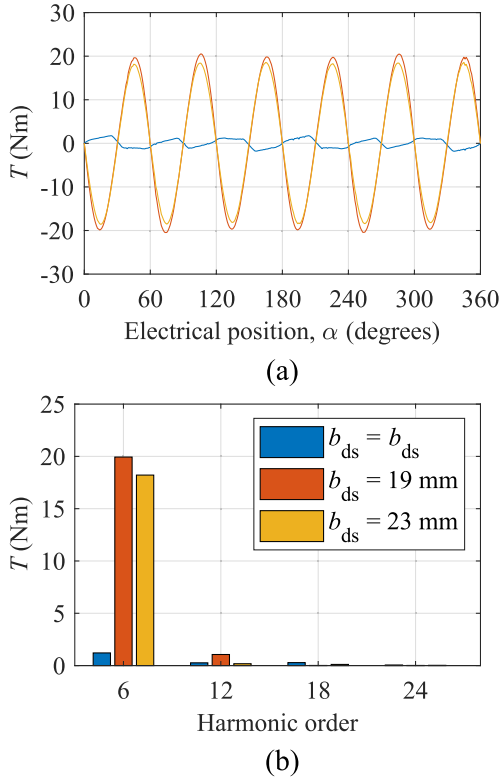

FIGURE 5. (a) Cogging torque for different values of the stator tooth inner width b_{ds} and (b) its spectra. 2D FEA.

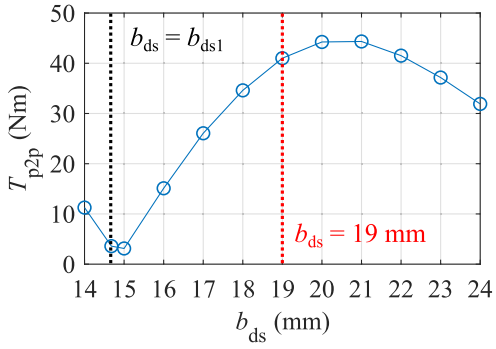

FIGURE 6. Cogging torque (peak-to-peak value) variation as a function of the stator tooth inner width b_{ds}. 2D FEA.

a comparison of the submersible core machine and the canned machine (having traditional electrical steel in the stator core) is provided.

A. LOSS CALCULATION

The stator winding Joule losses are calculated by (neglecting additional AC losses) [16], [29]

$$P_{\mathrm{Cu}} = k_{\mathrm{R}} Q_{\mathrm{s}} z_{\mathrm{Q}}^2 \rho_{\mathrm{Cu}} \left(\frac{l + l_{\mathrm{w}}}{S_{\mathrm{slot}} k_{\mathrm{Cu}}} \right) I_{\mathrm{s}}^2, \tag{3}$$

where k_{R} is the resistance factor, ρ_{Cu} is the copper resistivity at the operating temperature, z_{Q} is the number of conductors in one slot, k_{Cu} is the copper space factor, and l_{w} is the end winding length. It should be noted that the end-winding length depends on the stator tooth inner width b_{ds}. The typical procedure for calculating the low-frequency laminated core iron losses over an electric period is applied using the following expression (neglecting excess losses) [6]

$$P_{\mathrm{Fe}} = \sum_{n=1}^{N} k_{\mathrm{f}} \left(k_{\mathrm{h}} \hat{B}_n^2 f_{\mathrm{s}} A_n l + \frac{d^2}{12 \sigma_{\mathrm{Fe}}} \frac{1}{T} \int_0^T \left(\frac{\mathrm{d}B_n}{\mathrm{d}t} \right)^2 A_n l \, \mathrm{d}t \right), \tag{4}$$

where k_{f} is the iron space factor, k_{h} is the hysteresis loss coefficient, σ_{Fe} is the material conductivity, d is the material thickness, f_{s} is the electrical frequency, A_n is the area of the n^{th} stator element, $\hat{B}_n$ is the maximum flux density in the n^{th} stator element, B_n is the instantaneous flux density in the n^{th} stator element, and N is the number of elements in the stator core. The first term of (4) corresponds to the static hysteresis losses of the laminated steel and the second term to dynamic eddy-current losses, also known as dynamic classical losses of the laminated steel. However, the procedure requires a loss coefficient, which depends on the material. Another way to calculate the hysteresis losses is to estimate the energy density of the stator elements. This can be done by applying the Jiles–Atherton (JA) hysteresis model discussed in [30], [31]. This model is used to calculate minor and major hysteresis loops from the physical parameters of the magnetic materials and it is included in the simulation software used in this study; however, the user must provide the tensor parameters of the material. The hysteresis energy density for each element of the stator magnetic domain over one electrical cycle can be expressed as

$$E_n = \oint H_{xn} \mathrm{d}B_{xn} + \oint H_{yn} \mathrm{d}B_{yn}, \tag{5}$$

where H_{xn} and H_{yn} are the x and y components of the magnetic field strength on the n^{th} stator element, and B_{xn} and B_{yn} are the x and y components of flux density on the n^{th} stator element. The flux density, magnetic field strength, and position information of the stator nodes are extracted for each time step. The static hysteresis torque can be calculated as

$$T_{\mathrm{hyst}} = \frac{p}{2\pi} k_{\mathrm{f}} \sum_{n=1}^{N} E_n A_n l. \tag{6}$$

The hysteresis torque is resistive or detent torque [32]. Furthermore, being resistive torque, it is usually considered mechanical friction torque. However, based on the analysis presented above, this torque is caused by the hysteresis phenomenon of the iron core. Moreover, the hysteresis torque depends mainly on the magnetic properties of the material. The static hysteresis losses are given by

$$P_{\mathrm{hyst}} = T_{\mathrm{hyst}} \Omega, \tag{7}$$

where Ω is the mechanical angular velocity. The eddy-current losses can be computed with the second term of (4) from the

information extracted from the calculation of the hysteresis losses. The parameters related to the calculation of the classic losses (lamination thickness and material conductivity) are provided by the steel manufacturer (see Table 3). The accuracy of the iron loss calculation depends on the mesh quality. The eddy current loss in the rotor can be calculated in the FEA as

$$P_{\text{eddy}} = \int_V \frac{J^2}{\sigma} \mathrm{d}V, \tag{8}$$

where J is the current density in the material, and σ is the material conductivity. Equation (8) is valid for solid materials. In the FEA software, losses can be calculated by selecting the rotor solid tube and the magnets as solid conductor regions with their corresponding conductivities. Naturally, in the 2D simulation environment, the end effect is not directly included, which usually leads to higher estimated losses caused by the eddy currents.

The loss calculation takes into account the skewing effect. The losses are computed following a procedure similar to that of calculating torque ripple in skewed machines, described in [10].

The mechanical and additional losses are estimated using an empirical approach. The drag torque caused by water flowing through the air gap is relatively low because of the low rotational speed; therefore, the drag losses are neglected.

B. MACHINE PERFORMANCE

The electromagnetic torque, back-electromotive force (EMF), and losses were computed for different operating conditions. The calculation of the electromagnetic torque includes the hysteresis torque and torques caused by the eddy currents and friction.

The back-EMF at the rated mechanical speed as a function of the stator tooth inner width b_{ds} is shown in Fig. 7(a). The current at the rated load as a function of the stator tooth inner width b_{ds} is depicted in Fig. 7(b). It can be concluded from the results that it is possible to decrease the stator current by using the approach with unequal teeth widths because of the increase in the back-EMF, as it was predicted in the previous section.

The machine loss distribution at the rated load as a function of the stator tooth inner width b_{ds} is shown in Fig. 8(a). It can be seen that by increasing the value of b_{ds}, the rotor losses increase even though the stator current decreases. This is mainly due to the higher order harmonics of the air gap flux density produced by the new stator shape and the slot opening, as shown in Fig. 8(b). As it can be seen in Fig. 8(a), the iron losses in the stator are very high (representing approximately 15% of the rated power) for each value of b_{ds}, where the origin of almost all iron losses is the hysteresis losses. Here, the negative effect of using the stainless-steel stator lamination material can be seen, the origin of which will be discussed later. The PM losses are less than 0.6 W as shown in Fig. 8(a). This is supported by the relatively high

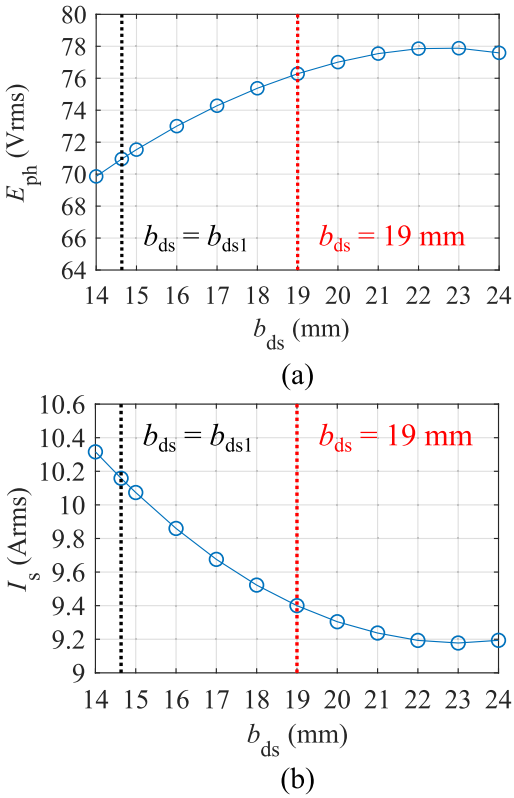

FIGURE 7. (a) RMS back-EMF value at the rated speed and (b) RMS stator current value at the rated load as a function of the stator tooth inner width b_{ds}. FEA.

electrical resistivity of the magnet material, low operating speed, and segmentation of the magnets.

The value chosen for b_{ds} is 19 mm. The criterion used to select the value of b_{ds} was also due to the rotor core losses, which increase with a higher b_{ds}. The rotor core losses are of significance because of the low heat transfer through the cover material.

The behavior of the machine with $b_{\text{ds}} = 19$ mm is compared with the original stator tooth inner width $b_{\text{ds}} = b_{\text{ds1}} = 14.67$ mm. Table 5 shows the components of the core losses for both cases. The hysteresis losses account for a significant proportion of the losses, which is manifested in a reduction in the actual output torque (around 30 Nm). The armature reaction has a major influence on the rotor losses because of the high harmonic content of the current linkage. Fig. 9 shows the total loss density distribution in the stator core region at the rated load for $b_{\text{ds}} = b_{\text{ds1}}$ and $b_{\text{ds}} = 19$ mm. It is observed that the area with the highest losses is found in the teeth that carry coils. However, this area represents only 25% of the total stator region. Therefore, iron losses will remain high as a result of the magnetic properties of the selected ferritic stainless steel regardless of the selected stator yoke depth.

A schematic view of the stainless machine and the completely canned machine is shown in Fig. 10. The canned machine consists of two covers in the air gap to protect the parts of the machine from contact with water. The stator and

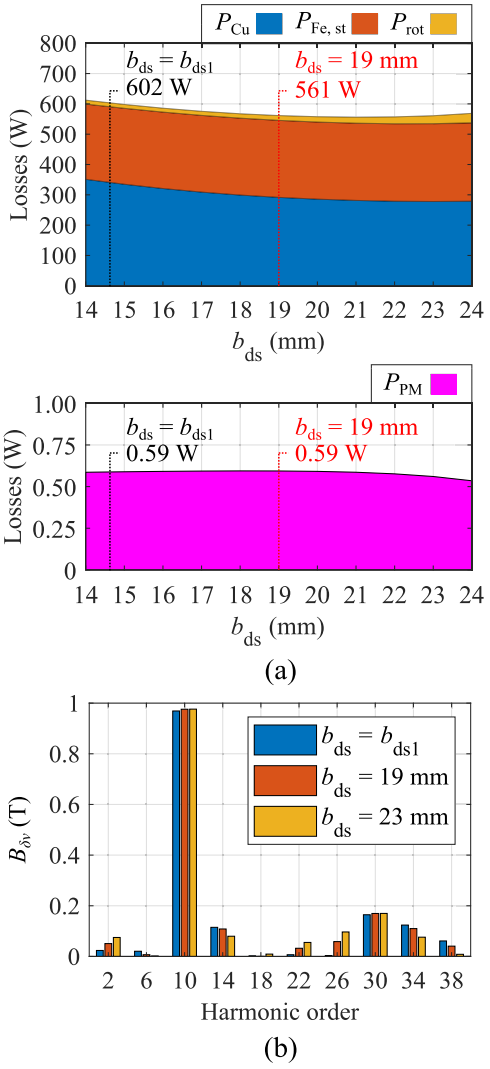

FIGURE 8. (a) Losses at the rated load as a function of the stator tooth inner width b_{ds} (P_{Cu}: stator winding Joule losses, $P_{Fe,st}$: stator iron losses, P_{rot}: rotor losses, P_{PM}: PM eddy-current loss) and (b) air gap flux density harmonics at the rated load for $b_{ds} = b_{ds1}$, $b_{ds} = 19$ mm, and $b_{ds} = 23$ mm. FEA.

TABLE 5. No-load and rated load electromagnetic losses for $b_{ds} = b_{ds1}$ and $b_{ds} = 19$ mm. FEA.

Parameter	$b_{ds} = b_{ds1}$	$b_{ds} = 19$ mm
Stator hysteresis loss[1] (W)	234.1	235.3
Stator eddy-current loss[1] (W)	3.6	3.5
Rotor losses[1] (W)	1.9	2.6
PM eddy-current loss[1] (W)	0.54	0.55
Stator winding losses[2] (W)	342.0	291.0
Stator hysteresis loss[2] (W)	247.9	249. 2
Stator eddy-current loss[2] (W)	3.8	3.7
Rotor losses[2] (W)	13.0	16.0
PM eddy-current loss[2] (W)	0.59	0.59

[1] $I_s = 0$ Arms, 80 rpm
[2] $I_s = I_{sN}$ Arms, 80 rpm

rotor cover thickness is 2.0 mm. The magnetic air gap length is 5.5 mm. The number of turns is set to the same value as in the proposed machine for a fair comparison. For both

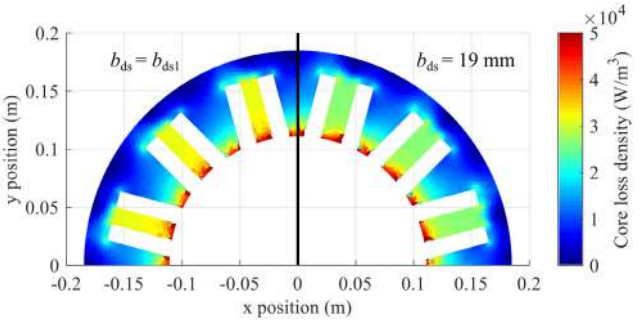

FIGURE 9. Core loss density distribution at the rated load for $b_{ds} = b_{ds1}$ (left) and $b_{ds} = 19$ mm (right). FEA.

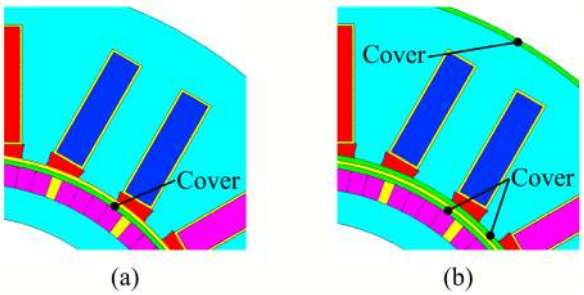

FIGURE 10. Schematic view of (a) the proposed machine and (b) the canned machine.

machines, skewing is considered in order to reduce cogging torque and torque ripple.

Fig. 11 shows the performance of both machines under a pump load profile $(T = k\Omega^2)$. The results show that the canned stator machine has a higher efficiency than the stainless machine up to 120 r/min. This is explained by the materials used in the stator cores and, in particular, by much smaller hysteresis losses in well-performing electrical steel compared with ferritic stainless steel. According to the information provided in Table 3, the coercivity of the ferritic stainless steel is about 14 times (700 A/m) as high as that of the traditional electrical steel, which results in a wide hysteresis loop. As shown in Fig. 11(a), the rated torque is achieved at similar currents in both machines even though the stator core materials are different, the M400-500 having a higher flux density than the 430SS at the same field strength (see Table 3). This can be explained by the fact that the stator inner diameter D_{si} in the machine with M400-50A (canned machine) was increased in comparison with the machine with a stainless steel core (proposed machine), which resulted in a larger effective air gap.

Even though the use of stainless-steel material in the stator core leads to a lower efficiency, its usage can be justified by the simpler overall stator structure, where the stator does not have to be protected from water penetration. Further, the stator filled with water has better cooling properties, especially at the end windings, which are directly surrounded by the fluid.

Table 6 provides the torque density and specific torque of both machines. The motor volumes are the same, whereas

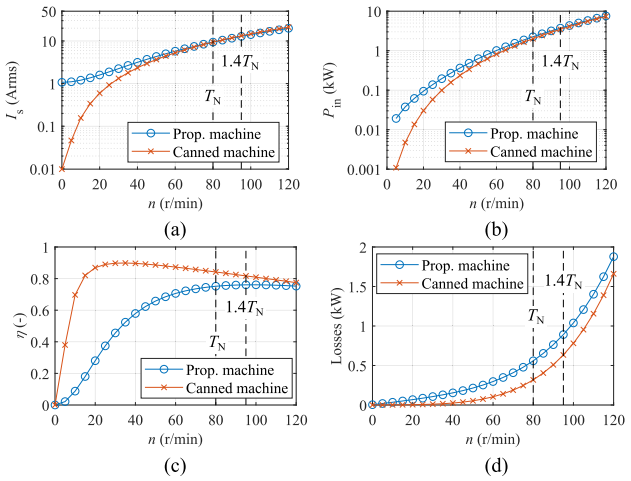

FIGURE 11. Load performance (pump load profile) of the proposed and canned machine: (a) stator current, (b) input power, (c) per unit efficiency, and (d) total losses as a function of speed. FEA.

TABLE 6. Torque densities and specific torques of the proposed and canned machine.

Parameter	Prop. machine	Canned machine
Current density at rated torque J_N (A/mm^2)	2.99	2.98
Volume V (m^3)	0.0280	
Mass m (kg)	181.0	175.1
Rated torque density TD_N (Nm/m^3)	$\sim 7.25\times10^3$	
Rated specific torque ST_N (Nm/kg)	1.12	1.16

the masses differ by 5.9 kg (the cover not included). The difference in the masses of these motors is due to the density of the stator materials. It is pointed out that the use of covers reduces the stator core volume in the canned machine because of the increase in the stator inner diameter D_{si} and because the stator outer diameter D_{se} is fixed by the application requirements. The rated torque is achieved at similar current densities as predicted above (see Fig. 11). This is explained by the extra effective air gap resulting from the additional stator cover in the canned machine and the somewhat reduced positive effect of using electromagnetic steel with higher saturation flux density in the stator core. Therefore, for the reasons mentioned above and because the motor volumes are identical, the torque densities are similar. In the case of the specific torque, the canned machine provides a higher value than the proposed machine because of the difference in mass; however, the difference in values is small.

Based on the previous analysis, it was decided to test this approach in a submersible motor application where the stator needs no protection against water penetration because of the water-tolerant materials. It is believed that alternative water-resistant materials (e.g., PVC winding and stainless steel core) can be successfully applied in systems that require high reliability. In this case, some sacrifice on efficiency should be accepted because of the relatively high hysteresis losses in the stainless steel core. Naturally, a low-coercivity

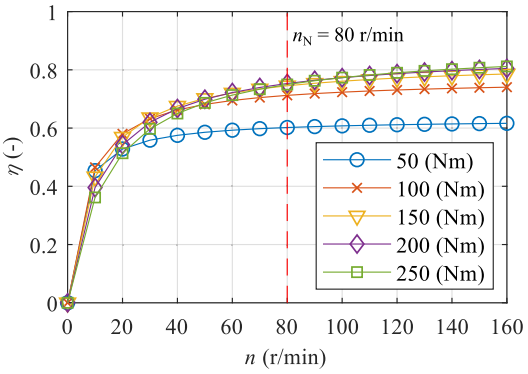

FIGURE 12. Efficiency of the proposed machine as a function of rotational speed at different load levels. FEA.

ferritic stainless steel would solve the problem. However, if the machine is evaluated at speeds higher than the nominal and at a constant torque, it is possible to observe an increased efficiency as shown in Fig. 12. Therefore, this result shows the potential of using an unconventional stator core material for low- and medium-speed applications.

IV. EXPERIMENTAL VALIDATION

A. PROTOTYPE MACHINE

When building the machine, its rotor core was constructed from a solid tube divided into two parts without significant difficulties. Fig. 13(a) shows a schematic of the PMs mounted on the rotor core. Each PM was divided into four segments per pole and four sections in the axial direction for easy manufacture and because of the two-step rotor skewing. Once the PMs were in place, the preformed GFRP cover was installed and voids were filled with epoxy resin. The assembled rotor is shown in Fig. 13(b). The stator core sheets and the assembled stator are shown in Fig. 14. Insulation between sheets was provided by a layer of epoxy glue between the sheets when the stack was formed. The open stator slots facilitated the mounting of preformed coils. The wire used in the coils was PVC-insulated wire with a solid conductor, an external diameter of 3.1 mm, and a copper diameter of 2.0 mm (copper cross-sectional area 3.14 mm^2). The wire arrangement in the stator slot is shown in Fig. 15(a). The PVC cover is not hard and deforms easily; therefore, the use of preformed coils is advisable to guarantee their condition before assembly in the stator slots. A 3D printed model of part of the machine (see Fig. 15(b)) was built to ensure that there is enough space in the stator slot for the preformed coil.

B. DESCRIPTION OF THE TEST BENCH

The schematic and a photograph of the test bench are shown in Fig. 16. The prototype is coupled to an induction machine (IM), which acts as a dynamometer. The prototype and the IM dynamometer are supplied by a frequency converter (ACS355 and ACS611, respectively). The prototype was driven with the $i_d = 0$ control. The layout of the test bench is vertical according to the requirements of the application. The prototype was immersed in a container with

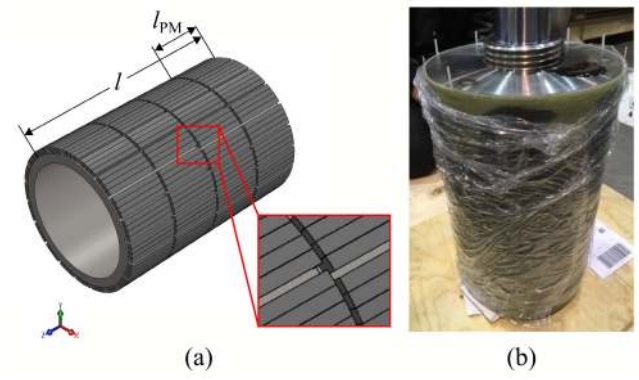

FIGURE 13. (a) View of stepped skewing (two steps) of the permanent magnet layers in the rotor and (b) canned rotor.

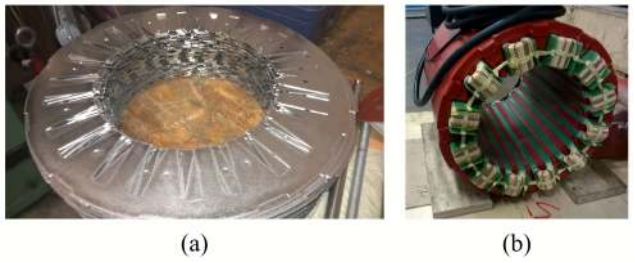

FIGURE 14. (a) Stator core sheets and (b) assembled stator.

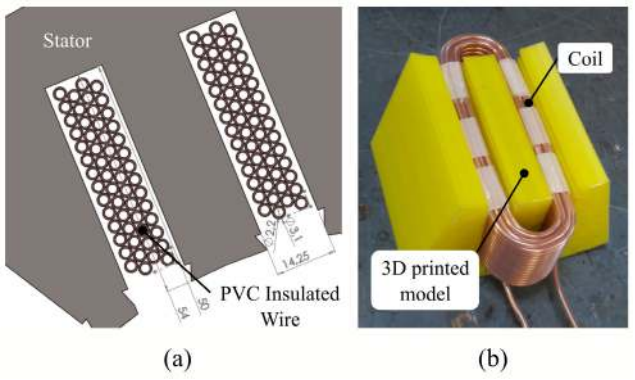

FIGURE 15. (a) Wire positions of one complete coil in the stator slots and (b) 3D printed model of a part of the stator core with a coil inserted.

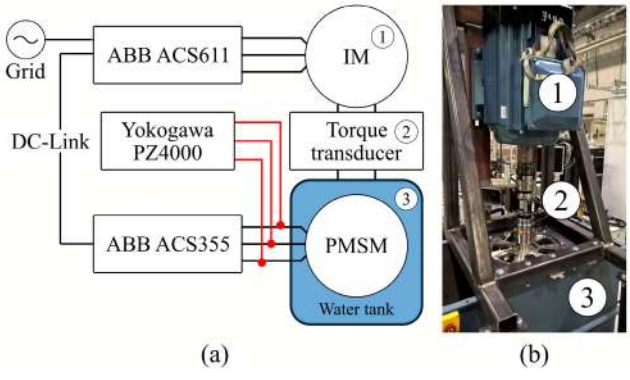

FIGURE 16. (a) Schematic and (b) a photograph of the experimental setup.

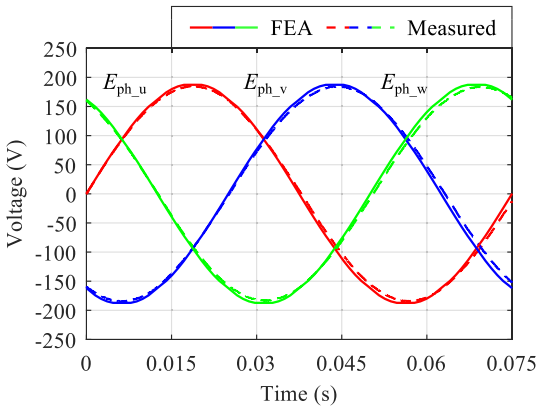

FIGURE 17. Comparison of the simulated and measured back-EMF waveforms at the rated speed.

TABLE 7. Machine losses at the rated point.

Parameter	Calculated	Measured
Copper losses (W)	291.0	291.0
Stator iron losses (W)	252.9	-
Rotor losses (W)	16.0	-
PM losses (W)	0.6	-
Friction + additional losses (W)	34.0	-
Total losses (W)	594.5	592.0
Efficiency (-)	0.74	0.74

water at room temperature to observe the behavior of the machine in water. A torque and speed transducer was coupled between the two machines. The voltage and current measurements in the prototype were performed with a Yokogawa PZ4000 Power Analyzer.

C. MEASUREMENTS

Fig. 17 depicts the simulated and measured waveforms of the back-EMF at the rated speed. The results show that the error (peak-to-peak voltage) between the FEA and the experimental test is around 4%, which is tolerable.

A constant resistive torque was measured at different speeds (no-load condition). The value obtained was approximately 30 Nm corresponding to the sum of hysteresis torque and friction. From the analysis presented in the previous section, it is possible to conclude that the hysteresis torque predicted by the FEA has a good agreement with the measured hysteresis torque.

The efficiency maps obtained by the FEA and measurements are shown in Fig. 18. The efficiency behavior is similar for the estimated and measured maps. Furthermore, the maximum value of efficiency is reached when the machine operates in its rated condition. Table 7 shows the distribution of machine losses in the rated operation. The efficiency can be considered somewhat low, which is a result of the very low operating speed and the stainless steel stator core, the hysteresis losses of which comprise a significant proportion of the total losses.

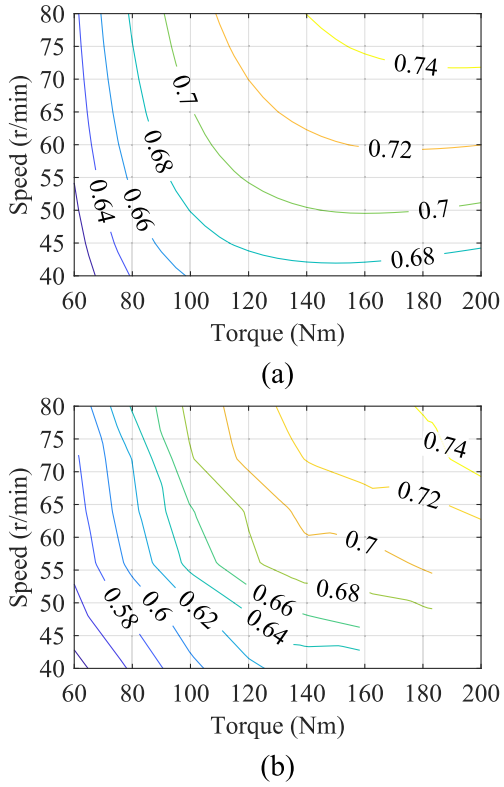

FIGURE 18. **(a) Simulated and (b) measured efficiency maps.**

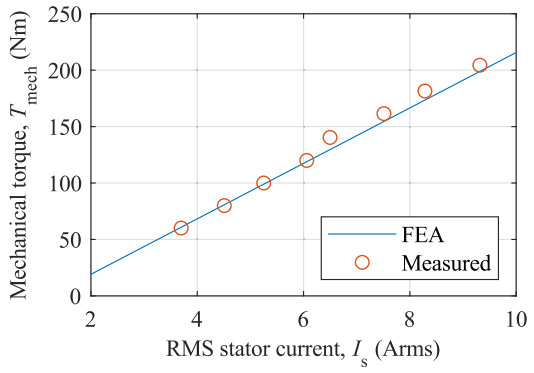

FIGURE 19. **Simulated and measured mechanical torque at the rated speed as a function of RMS stator current.**

Fig. 19 compares the calculated and measured mechanical torques at the rated speed for different RMS stator currents. As can be seen, there is a good agreement between the experiment and the simulation results.

During the measurements of the machine in operation, the water was flowing in the tank and its temperature was kept constant at about room temperature. Additionally, it was verified that during the testing, the machine operated without problems. Considering the relatively low losses of the machine size in question and the fact that the windings were submerged, it is unlikely that there was a significant difference between the winding and water temperatures. Unfortunately, it was not possible to arrange accurate temperature distribution measurements with the machine in operation. Nevertheless, according to the measurement results during the long-running operation, the supply voltage and current values did not change. Therefore, it was assumed that the resistance of the winding remained at the same level, which verified that the temperatures of the winding and the permanent magnets did not rise significantly when the motor was running for several hours.

V. CONCLUSION

This paper presented a stainless submersible permanent magnet synchronous machine. The proposed machine was evaluated by the FEA and compared with a stator canned machine. The submersible machine with ferritic stainless steel was shown to be functional and can be considered an alternative to traditional electrical steels in a special application. Ferritic stainless steels have acceptable magnetic properties and are readily available in the market. However, because of its high coercivity, the material generates significant hysteresis torque. Therefore, should there be a ferritic stainless steel with acceptably low coercivity, it would solve the problem of high hysteresis losses and make this material very attractive for electrical machines operated in harsh environments. In the case of a completely canned machine, it is possible to protect traditional electric steel from contact with water with a special cover, but with the penalty of a less reliable overall stator structure and the risk of the can failing over time.

ACKNOWLEDGMENT

Alvaro E. Hoffer wishes to thank the University of Concepción, Chile, and LUT University, Finland, for supporting his Ph.D. studies.

The authors would like to thank Dr. Hanna Niemelä, LUT University, Finland, for her linguistic assistance in the preparation of this manuscript.

REFERENCES

[1] Q. Yu, S. Chu, W. Li, L. Tian, X. Wang, and Y. Cheng, "Electromagnetic shielding analysis of a canned permanent magnet motor," *IEEE Trans. Ind. Electron.*, vol. 67, no. 10, pp. 8123–8130, Oct. 2020.

[2] F. Wani, H. Polinder, J. Dong, and A. Yadav, "Comparing different materials for rotor-can in flooded generators," in *Proc. 23rd Int. Conf. Electr. Mach. (ICEM)*, Sep. 2018, pp. 2572–2578.

[3] S. Sashidhar and B. G. Fernandes, "A novel ferrite SMDS spoke-type BLDC motor for PV bore-well submersible water pumps," *IEEE Trans. Ind. Electron.*, vol. 64, no. 1, pp. 104–114, Jan. 2017.

[4] P. Oxley, J. Goodell, and R. Molt, "Magnetic properties of stainless steels at room and cryogenic temperatures," *J. Magn. Magn. Mater.*, vol. 321, no. 14, pp. 2107–2114, Jul. 2009.

[5] T. Judendorfer, J. Fletcher, N. Hassanain, M. Mueller, and M. Muhr, "Challenges to machine windings used in electrical generators in wave and tidal power plants," in *Proc. Conf. Electr. Insul. Dielectr. Phenomena (CEIDP)*, Aug. 2009, pp. 238–241.

[6] I. Petrov and J. Pyrhönen, "Performance of low-cost permanent magnet material in PM synchronous machines," *IEEE Trans. Ind. Electron.*, vol. 60, no. 6, pp. 2131–2138, Jun. 2013.

[7] P. Ponomarev, Y. Alexandrova, I. Petrov, P. Lindh, E. Lomonova, and J. Pyrhönen, "Inductance calculation of tooth-coil permanent-magnet synchronous machines," *IEEE Trans. Ind. Electron.*, vol. 61, no. 11, pp. 5966–5973, Nov. 2014.

[8] P. Lindh, J. Montonen, P. Immonen, J. A. Tapia, and J. Pyrhönen, "Design of a traction motor with tooth-coil windings and embedded magnets," *IEEE Trans. Ind. Electron.*, vol. 61, no. 8, pp. 4306–4314, Aug. 2014.

[9] E. Carraro, N. Bianchi, S. Zhang, and M. Koch, "Design and performance comparison of fractional slot concentrated winding spoke type synchronous motors with different slot-pole combinations," *IEEE Trans. Ind. Appl.*, vol. 54, no. 3, pp. 2276–2284, May 2018.
[10] I. Petrov, P. Lindh, M. Niemela, E. Scherman, and J. Pyrhonen, "High-torque-density IPMSM rotor pole geometry adjustment for smooth torque," *IEEE Access*, vol. 7, pp. 52650–52658, 2019.
[11] A. M. EL-Refaie, "Fractional-slot concentrated-windings synchronous permanent magnet machines: Opportunities and challenges," *IEEE Trans. Ind. Electron.*, vol. 57, no. 1, pp. 107–121, Jan. 2010.
[12] N. Bianchi, S. Bolognani, and M. D. Pré, "Magnetic loading of fractional-slot three phase PM motors with non-overlapped coils," in *Proc. Conf. Rec. IAS Annu. Meeting (IEEE Ind. Appl. Soc.)*, vol. 1, Oct. 2006, pp. 35–43.
[13] D. Ishak, Z. Q. Zhu, and D. Howe, "Permanent-magnet brushless machines with unequal tooth widths and similar slot and pole numbers," *IEEE Trans. Ind. Appl.*, vol. 41, no. 2, pp. 584–590, Mar. 2005.
[14] I. Petrov, P. Ponomarev, Y. Alexandrova, and J. Pyrhönen, "Unequal teeth widths for torque ripple reduction in permanent magnet synchronous machines with fractional-slot non-overlapping windings," *IEEE Trans. Magn.*, vol. 51, no. 2, pp. 1–9, Feb. 2015.
[15] I. Petrov, P. Ponomarev, and J. Pyrhönen, "Asymmetrical geometries in electrical machines," *Int. Rev. Electr. Eng.*, vol. 11, no. 1, p. 20, Feb. 2016.
[16] J. Pyrhönen, T. Jokinen, and V. Hrabovcova, *Design of Rotating Electrical Machines*. Hoboken, NJ, USA: Wiley, Oct. 2013.
[17] A. E. Hoffer, J. A. Tapia, I. Petrov, and J. Pyrhonen, "Design of a stainless core submersible permanent magnet generator for tidal energy," in *Proc. 45th Annu. Conf. IEEE Ind. Electron. Soc. (IECON)*, Oct. 2019, pp. 1010–1015.
[18] G. Pellegrino, A. Vagati, P. Guglielmi, and B. Boazzo, "Performance comparison between surface-mounted and interior PM motor drives for electric vehicle application," *IEEE Trans. Ind. Electron.*, vol. 59, no. 2, pp. 803–811, Feb. 2012.
[19] Z. Q. Zhu and D. Howe, "Influence of design parameters on cogging torque in permanent magnet machines," *IEEE Trans. Energy Convers.*, vol. 15, no. 4, pp. 407–412, Dec. 2000.
[20] N. Bianchi, S. Bolognani, and E. Fornasiero, "An overview of rotor losses determination in three-phase fractional-slot PM machines," *IEEE Trans. Ind. Appl.*, vol. 46, no. 6, pp. 2338–2345, Nov. 2010.
[21] H. V. Xuan, D. Lahaye, H. Polinder, and J. A. Ferreira, "Influence of stator slotting on the performance of permanent-magnet machines with concentrated windings," *IEEE Trans. Magn.*, vol. 49, no. 2, pp. 929–938, Feb. 2013.
[22] I. Petrov, M. Niemela, P. Ponomarev, and J. Pyrhönen, "Rotor surface ferrite permanent magnets in electrical machines: Advantages and limitations," *IEEE Trans. Ind. Electron.*, vol. 64, no. 7, pp. 5314–5322, Jul. 2017.
[23] T. Aho, V. Sihvo, J. Nerg, and J. Pyrhönen, "Rotor materials for medium-speed solid-rotor induction MotorS," in *Proc. IEEE Int. Electr. Mach. Drives Conf. (IEMDC)*, vol. 1, May 2007, pp. 525–530.
[24] M.-S. Lim, S.-H. Chai, J.-S. Yang, and J.-P. Hong, "Design and verification of 150-krpm PMSM based on experiment results of prototype," *IEEE Trans. Ind. Electron.*, vol. 62, no. 12, pp. 7827–7836, Dec. 2015.
[25] Arnold Magnetic Technologies. (2017). *N45SH Datasheet*. [Online]. Available: https://www.arnoldmagnetics.com/wp-content/uploads/2017/11/N45SH-151021.pdf
[26] I. Petrov, P. Lindh, and J. Pyrhönen, "Importance of accurate iron permeability in saturated condition on performance evaluation of flux-switching permanent magnet synchronous machines," *IEEE Trans. Magn.*, vol. 54, no. 6, pp. 1–7, Jun. 2018.
[27] Cogent Power Ltd. (2009). *Typical Data for SURA M400-50A0*. [Online]. Available: https://cogent-power.com/cms-data/downloads/m400-50a.pdf
[28] B. Janjic, A. Binder, V. Bischof, and G. Ludwig, "Design of PM integrated motor-drive system for axial pumps," in *Proc. Eur. Conf. Power Electron. Appl. (EPE)*, 2007, pp. 1–10.
[29] A. E. Hoffer, I. Petrov, J. Pyrhönen, J. A. Tapia, and G. Bramerdorfer, "Analysis of a tooth-coil winding permanent-magnet synchronous machine with an unequal teeth width," *IEEE Access*, vol. 8, pp. 71512–71524, 2020.
[30] S. Hussain and D. A. Lowther, "The modified Jiles–Atherton model for the accurate prediction of iron losses," *IEEE Trans. Magn.*, vol. 53, no. 6, pp. 1–4, Jun. 2017.
[31] R. Du and P. Robertson, "Dynamic Jiles–Atherton model for determining the magnetic power loss at high frequency in permanent magnet machines," *IEEE Trans. Magn.*, vol. 51, no. 6, pp. 1–10, Jun. 2015.
[32] S.-W. Hwang, M.-S. Lim, and J.-P. Hong, "Hysteresis torque estimation method based on iron-loss analysis for permanent magnet synchronous motor," *IEEE Trans. Magn.*, vol. 52, no. 7, pp. 1–4, Jul. 2016.

ALVARO E. HOFFER (Student Member, IEEE) was born in Temuco, Chile, in 1991. He received the B.Eng. and M.Eng. degrees in electrical engineering from the Universidad de La Frontera, Temuco, Chile, in 2016. He is currently pursuing the Ph.D. degree with the Department of Electrical Engineering, University of Concepción, Chile, and the Department of Electrical Engineering, LUT University, Finland, through a double degree (DD) agreement. His current research interests include the field of electrical machines and drives, and renewable energies.

ILYA PETROV received the D.Sc. degree from the Lappeenranta University of Technology (LUT), Finland, in 2015. He is currently a Researcher with the Department of Electrical Engineering, LUT.

JUHA J. PYRHÖNEN (Senior Member, IEEE) was born in Kuusankoski, Finland, in 1957. He received the D.Sc. degree from the Lappeenranta University of Technology (LUT), Finland, in 1991. He became an Associate Professor of Electrical Engineering with LUT, in 1993, and a Professor of Electrical Machines and Drives, in 1997. He is engaged in research and development of electric motors and electric drives. His current research interests include different synchronous machines and drives, induction motors and drives, and solid-rotor high-speed induction machines and drives.

JUAN A. TAPIA (Senior Member, IEEE) received the B.Sc. and M.Sc. degrees in electrical engineering from the University of Concepción, Concepción, Chile, in 1991 and 1997, respectively, and the Ph.D. degree from the University of Wisconsin–Madison, Madison, WI, USA, in 2002. From 2010 to 2014, he was a FiDiPro Fellow with the Academy of Finland, Lappeenranta University of Technology, Lappeenranta, Finland, where he conducted research on PM machines with LUT Energy. He is currently working as a Professor with the Department of Electrical Engineering, University of Concepción. His research interests include electrical machine design, numerical methods for electromagnetic fields, and renewable energy.